In-Plane and Out-of-Plane Defectivity in Thin Films of Lamellar Block Copolymers

NIKHILA MAHADEVAPURAM a,‡ , INDRANIL MITRA b,‡ , ALONA BOZHCHENKO a , JOSEPH

STRZALKA b , GILA E. STEIN a,*

^a Department of Chemical and Biomolecular Engineering, University of Houston, Houston, TX

77204-4004

^b X-Ray Science Division, Argonne National Laboratory, Argonne, IL 60439

*gestein@uh.edu

† Equally contributing authors.

Dated: September 28, 2015

1

ABSTRACT: We investigate the ordering of poly(styrene-b-methyl methacrylate) (PS-PMMA) lamellar copolymers (periodicity $L_0 = 46$ nm) confined between a free surface and brushed poly(styrene-r-methyl methacrylate) silicon substrate. The processing temperature was selected to eliminate wetting layers at the top and bottom interfaces, producing approximately neutral boundaries that stabilize perpendicular domain orientations. The PS-PMMA film thickness $(t=0.5L_0-2.5L_0)$ and brush grafting density $(\Sigma=0.2-0.6~{
m nm}^{-2})$ were systematically varied to examine their impacts on in-plane and out-of-plane ordering. Samples were characterized with a combination of high resolution microscopy, x-ray reflectivity, and grazing-incidence small angle X-ray scattering. In-plane order at the top of the film (quantified through calculation of orientational correlation lengths) improved with t^n , where the exponent n increased from 0.75 to 1 as Σ decreased from 0.6 to 0.2 nm⁻². Out-of-plane defects such as tilted domains were detected in all films, and the distribution of domain tilt angles was nearly independent of t and Σ . These studies demonstrate that defectivity in perpendicular lamellar phases is three-dimensional, comprised of in-plane topological defects and out-of-plane domain tilt, with little or no correlation between these two types of disorder. Strong interactions between the block copolymer and underlying substrate may trap both kinds of thermally-generated defects.

Keywords: Block Copolymers, Thin films, Grazing Incidence Small Angle X-ray Scattering, Directed Self Assembly, Defectivity

INTRODUCTION

Thin films of symmetric diblock copolymers can spontaneously self-assemble into nanoscale lamellar domains (i.e., nanolines). ^{1,2} These materials could improve the resolution of projection lithography by "shrinking" the sizes of patterned features, ³⁻⁶ so leading semiconductor manufacturers are considering their use in next-generation integrated circuit manufacturing. Lithographic processes require precise control over the placement and orientation of domains with respect to the underlying substrate. While many methods have been developed to direct the placement of domains, the in-plane and out-of-plane defectivity remains too high for production. The objective of our current work is to examine in-plane and out-of-plane defect structures in thin films of perpendicular poly(styrene-*b*-methyl methacrylate) (PS-PMMA) lamellae. In-plane defects are well-documented in these systems, and they include dislocations and disclinations that disrupt lateral order. Out-of-plane defects are not well-studied, but could include tilted, bent, or discontinuous domains.

Lithography requires nanopatterns in the plane of the film, so lamellar domains must be oriented perpendicular to the substrate. The perpendicular orientation is stable when the free surface and substrate are energetically "neutral" with respect to each block, so there is no tendency to form wetting layers at either interface. There are well-documented processing schemes that achieve interfacial neutrality in systems of lamellar PS-PMMA copolymers: elevated processing temperature generates a neutral air interface, 7-10 and the substrate chemistry can be tuned with established protocols to screen preferential adsorption of one block. 11-16 However, subtle changes in interactions at the free surface or substrate could impact both in-plane and out-of-plane defectivity.

Perpendicular lamellae and parallel cylinders are both examples of smectic block copolymer phases, and their in-plane ordering on homogeneous surfaces has been extensively studied through theory and experiment. ^{17–22} Fingerprint patterns are characterized by thermally-generated dislocations and disclinations, and the densities of these topological defects will increase with proximity to the order-disorder transition temperature. The phase behavior and defectivity in these systems are both sensitive to thin film confinement and types of interfacial interactions. In perpendicular lamellar phases, the order-disorder transition temperature can vary with the composition of

neutral substrate coatings, ²³ and defect densities increase as film thickness is reduced. ^{22,24,25} Similarly, confinement of parallel cylinders in a monolayer can suppress the order-disorder transition temperature and increase the defect densities, ²¹ with the maximum disorder detected on adsorbed brushes compared with grafted brushes. ^{26,27} Adsorbed brushes are thought to have lower chain densities (per unit area) than grafted brushes, and are therefore less effective at screening interactions between a substrate and overlying copolymer film.

Out-of-plane order in perpendicular block copolymer phases has received little attention in experiments, but there is evidence that domains are not perfectly vertical with respect to the substrate. One work used detailed studies of pattern transfer to show that perpendicular cylinders can tilt and bend, ²⁸ which was described as a response to the strain field associated with in-plane topological defects. A different study used grazing-incidence small angle X-ray scattering to show tilting and bending in perpendicular lamellae, ⁹ and this behavior was attributed to weakly preferential interactions at the substrate. Much of the current understanding of three-dimensional order is derived from theoretical models. ²⁹ For example, a variety of simulation methods predict that preferential interactions at a boundary can locally deform domain shapes and introduce complex morphologies, ^{6,30–33} and some of these features have been verified in experiments. ^{6,32} More generally, out-of-plane disorder might be intrinsic to these soft lamellar phases: As discussed in the preceding paragraph, the thermal generation of in-plane defects is well-documented in the literature, so it is very unlikely that these systems spontaneously assemble into perfectly vertical domains.

This manuscript examines in-plane and out-of-plane defectivity in thin films of PS-PMMA lamellar copolymers (periodicity $L_0=46$ nm) prepared on end-grafted poly(styrene-r-methyl methacrylate) brushes. The principal experimental variables are normalized PS-PMMA film thickness (t/L_0) and brush grafting density (Σ) . While t/L_0 is a common variable for investigations of thin film self-assembly, the impact of Σ on lamellar ordering is far less studied, 30,31 and this parameter is rarely reported in experiments. Brushes with a range of Σ are prepared by varying the kinetics of the grafting-to reaction, 34 and Σ is quantified through X-ray reflectivity (XRR) measurements of the dry brush thickness. 34,35 PS-PMMA films are processed at an elevated temperature that eliminates wetting layers at both interfaces. Through detailed analysis of surface microscopy and grazing-incidence small angle X-ray scattering (GISAXS), we find that all films

are characterized by high densities of thermally-generated in-plane and out-of-plane defects such as dislocations, disclinations, and tilted domains. Defectivity increases when ordering is most sensitive to confinement and interactions with the underlying substrate, which occurs in ultrathin films on brushes with low Σ .

EXPERIMENTAL PROCEDURES

Materials. The diblock copolymer used for these studies is a lamellar poly(styrene-b-methyl methacrylate) (PS-PMMA). The equilibrium lamellar periodicity (L_0) for this PS-PMMA copolymer is 46 nm (measured with grazing-incidence small angle X-ray scattering). The segregation strength for this polymer is $\chi N \simeq 45$ and approximately independent of temperature. ³⁶ Polymer brushes were prepared from hydroxyl-terminated poly(styrene-r-methyl methacrylate) random copolymers, hereafter denoted by P(S-r-MMA), and materials were selected based on the optimal compositions/molecular weights reported by others. ^{13,37} All polymers were purchased from Polymer Source and independently characterized at the University of Houston. The compositions, molecular weights, and dispersities are reported in Table 1. Substrates were 3-inch diameter p-type (100)-oriented silicon wafers. Substrates were cleaned with a UVOCS UV/ozone system for 20 mins to destroy organic contamination and grow a thin oxide layer.

Polymer	Styrene %	M_n (kDa)	Ð
PS-PMMA	53% vol	98	1.1
P(S-r-MMA)	59% mol	8.6	1.5
P(S-r-MMA)	55% mol	7	1.3

Table 1: Material characteristics. M_n is number-average molecular weight, and D is dispersity.

Brush Preparation. The end-functional random copolymers were dissolved in toluene at a concentration of 1 wt%, and films were prepared by spin-casting on clean silicon wafers. The film thicknesses were approximately 30 nm for each sample. Polymer chains were grafted to the substrate by annealing under low vacuum (10 mTorr) or in a nitrogen-purged glove box for

the temperature and time reported in Table 2. Processing conditions were varied to control the thickness of the polymer brushes (annealing temperature T, annealing time τ). Un-grafted polymer was extracted by soaking in toluene with mild agitation. Samples were then dried under a nitrogen stream. The quality of each brush was assessed by measuring the contact angle of water, which was as low as 76° after this process. Contact angle was increased to ca. 80° by repeating all steps a second time (includes coating a new film, annealing, and rinsing), which improves the homogeneity of the coating across the wafer surface. This contact angle is consistent with other literature studies, 23,37 and does not change by repeating all steps a third time.

Brush	T(°C)	τ (hr)	$t_b \; (\mathrm{nm})$
55% S	170	48	6.2 ± 0.1
55% S	170	24	4.8 ± 0.1
55% S	230	1	4.4 ± 0.1
55% S	210	1.5	3.4 ± 0.1
59% S	170	48	2.6 ± 0.1

Table 2: Brush thicknesses (t_b) determined with X-ray reflectivity (XRR). Processing conditions (T, τ) are reported for each brush system.

Brush Thickness. The brush thicknesses were measured using X-ray reflectivity (XRR). XRR experiments were performed at the Advanced Photon Source of Argonne National Laboratory (beamline 8-ID-E). B Data were acquired by varying the incident angle in the range of $0.1-2^{\circ}$ using increments of 0.003° , and the intensity at specular reflection $(2\Theta=0)$ was recorded with an avalanche photodiode detector. XRR data were modeled following the Parratt recursions convolved with an instrumental resolution function, where brush thickness (t_b) , brush scattering length density (ca. 10.1×10^{-10} cm⁻²), and native oxide thickness (ca. 1 nm) were refined through regression analysis. The exact algorithm is described in detail elsewhere. The fits to XRR data are included in the Figure S1. The brush thicknesses that were calculated from XRR are reported in Table 2. The uncertainties reported in Table 2 for t_b reflect the statistically-derived error. The

brush scattering length density was consistent among all samples, and corresponds with a mass density of $\rho \approx 1.1$ g/cm³.⁴¹

Surface Energy. The surface energies of all polymer brushes were calculated from equilibrium contact angle measurements based on Wu's harmonic method. 42,43 Four liquids were used: di-iodomethane (non-polar), deionized water (polar), ethylene glycol (polar), and formamide (polar). Contact angles were recorded from at least three points on the substrate using a DataPhysics OCA 15EC goniometer. We report the average and standard deviation in Table 3. Control measurements were performed from thin films of PS and PMMA homopolymer (ca. 50 nm). The PS has M_n of 140 kDa and $\mathcal D$ of 1.6, and the PMMA has M_n of 60 kDa and $\mathcal D$ of 1.4. The water contact angle of PS and PMMA homopolymers are $(90\pm1)^\circ$ and $(70\pm1)^\circ$, respectively.

PS-PMMA Thin Films. Thin films of PS-PMMA block copolymers were prepared on the P(S-r-MMA) brushes. PS-PMMA was dissolved in toluene at concentrations that ranged from 1-4 wt%, and solutions were filtered with a 0.2 μ m Teflon mesh. Films that ranged in thickness from 20 nm to 120 nm were prepared by spin-casting and annealed as described in the Results and Discussion. Polymer film thicknesses were measured with XRR following similar procedures as described for characterization of brush thickness. The PS-PMMA block copolymer film and underlying P(S-r-MMA) brush are modeled as a single layer with a scattering length density of ca. 10×10^{-10} cm⁻². (The brush thickness was characterized after the grafting reaction, so this value is subtracted from the "polymer layer" thickness to determine the PS-PMMA layer thickness.)

Microscopy. The nanoscale structure at the surface of each film was characterized with atomic force microscopy (AFM) and/or scanning electron microscopy (SEM). AFM micrographs were collected with a MultiMode 3 (Veeco) in Tapping Mode using silicon probes with a spring constant of approximately 40 N/m. Typical parameters for data acquisition were 1.7 Hz scan frequency, 5 μ m scan area, and 512 \times 512 image resolution. SEM images were recorded with a FEI XL-30FEG SEM in secondary electron (SE) mode. Operating parameters for image acquisition were an accelerating voltage of 5 kV, beam current of 95 pA, working distance of 5 mm, and magnifications ranging from 50-65 kx. Lateral domain order was quantified by calculating the

orientational correlation function. The exact algorithm is described elsewhere: ¹⁹ In brief, each image is converted to a gray scale format, and the orientation field $\theta(\vec{r})$ is determined by measuring the local intensity gradient. ¹⁸ The orientation direction is referenced to the horizontal axis. The order parameter is defined as $\Psi(\vec{r}) = \exp\{2i\theta(\vec{r})\}$, and the orientational correlation function is $g(\vec{r}) = \Psi^*(0)\Psi(\vec{r})$. The azimuthal average of $g(\vec{r})$ was fit to an exponential decay, i.e., $g(r) = \exp(-r/\zeta)$. ^{17–19} The orientational correlation length ζ was computed from a minimum of 5 micrographs and is normalized by $L_0 = 46$ nm. We report the average values with error bars that encompass ± 1 standard deviation, and in some cases the error bars are the same size as the symbols. We verified that ζ values calculated from AFM and SEM are identical within error (see Figure S2).

Grazing-Incidence Small Angle X-Ray Scattering (GISAXS). GISAXS measurements of PS-PMMA films were conducted at the Advanced Photon Source of Argonne National Laboratory (beamline 8-ID-E). Samples were placed in a vacuum chamber and illuminated with 7.35 keV radiation at incident angles (α^i) in the range of $0.1-0.24^\circ$. The off-specular scattering was recorded with a Pilatus 1MF pixel array detector (pixel size = 172 μ m) positioned 2175 mm from the sample. Acquisition times were approximately 10 sec per frame. Each data set was stored as a 981×1043 32-bit tiff image with 20-bit dynamic range. The X-ray penetration depth varies from approximately 10 nm up to the full film thickness as incident angle is increased through the critical angle of the film (ca. 0.17°). All data in this manuscript are displayed as intensity maps $I(2\Theta, \alpha^f)$, where 2Θ and α^f denote in-plane and out-of-plane scattering angles, respectively. Analysis methodology is discussed in the Appendix.

Rocking Curves. Rocking curves were recorded at the Advanced Photon Source of Argonne National Laboratory (beamline 8-ID-E) to quantify the effects of wafer curvature on incident beam angle, which is necessary for quantitative analysis of GISAXS data with the distorted-wave Born approximation. 44 Measurements were implemented by setting the incident angle to 0.4° and scanning an avalanche photodiode detector about the specular condition (from 0.35-0.45° in increments of 0.003°). Data were fit to a Gaussian resolution function,

$$R(q_z) = \frac{1}{\sqrt{2\pi}\delta_{q_z}} \exp\left(-\frac{q_z^2}{2\delta_{q_z}^2}\right),\tag{1}$$

where $q_z=2\pi(\sin[\alpha^f]+\sin[\alpha^i])/\lambda$ is the perpendicular scattering vector (out of plane) and $\delta_{q_z}=(\Delta\lambda/\lambda)q_z+4\pi\Delta\alpha^i/\lambda$. The wavelength spread is $\Delta\lambda/\lambda=10^{-4}$ (fixed), ³⁸ and the angular divergence of the beam $(\Delta\alpha^i)$ is an adjustable parameter for regression analysis. The angular divergence is typically 5×10^{-5} rad for a 400 μ m thick silicon wafer.

RESULTS AND DISCUSSION

The aim of these studies is to examine in-plane and out-of-plane defectivity in lamellar PS-PMMA block copolymers on brushed P(S-r-MMA) substrates. Samples were annealed at 240 °C, a temperature that suppresses the formation of wetting layers at each interface and drives a rapid self-assembly process. ⁴⁵ First, we describe the preparation and characterization of brushed P(S-r-MMA) substrates with a range of grafting density Σ . We show that the boundaries are effectively neutral at 240 °C, but there is evidence that PMMA is weakly attracted to the substrate. Second, we use quantitative analysis of surface microscopy to show that lateral order at the PS-PMMA/air interface improves with increasing film thickness and high brush grafting density. Third, we use quantitative analysis of GISAXS data to show that all samples are characterized by out-of-plane disorder in the form of tilted domains. This tilting behavior is nearly independent of film thickness and brush grafting density, although the broadest distribution of domain orientations is detected when Σ is low. Collectively, these data demonstrate that in-plane and out-of-plane defects are not strongly coupled, although both types of disorder can be trapped through interactions with the underlying substrate.

Substrate Preparation. All PS-PMMA films were cast on silicon wafers that were functionalized with random copolymer P(S-r-MMA) brushes, and substrate interactions were tuned by varying the brush grafting density. The grafting density Σ for each sample was calculated from the measured brush thickness t_b ,

$$\Sigma = \frac{t_b \rho N_A}{M_n},\tag{2}$$

where ρ is the approximate polymer density, N_A is Avogadro's number, and M_n is the number-average molecular weight.³⁴ Using the brush thicknesses and density calculated from XRR ($\rho = 1.1 \, {\rm g/cm^3}$), we predict that Σ ranges from approximately 0.2 nm⁻² to 0.6 nm⁻². These calculations

are summarized in Table 3. (If we base the calculation of Σ on weight-average molecular weight instead of M_n , then the estimated value drops by approximately 0.1 nm⁻² in each case.) The brushes prepared for this work span a broad range in Σ , but the wettability and surface energy (dispersive, polar, and total) determined with contact angle goniometry were consistent among all samples, and area always intermediate to those of PS and PMMA homopolymers. 42,43,46–49 Clearly, these measurements cannot detect small variations in brush structure.

Brush	$t_b \text{ (nm)}$	$\Sigma \; (\mathrm{nm}^{\text{-}2})$	H ₂ O (°)	$C_2H_6O_2$ (°)	CH ₃ NO (°)	CH ₂ I ₂ (°)	$\gamma \; ({ m mN/m})$
55% S	6.2 ± 0.1	0.59 ± 0.01	82 ± 1	61 ± 1	70 ± 1	27 ± 1	42.2 ± 0.7
55% S	4.8 ± 0.1	0.45 ± 0.01	83 ± 1	61 ± 1	70 ± 1	25 ± 3	42.6 ± 0.5
55% S	4.3 ± 0.1	0.41 ± 0.01	79 ± 1	61 ± 1	67 ± 1	27 ± 1	42.9 ± 0.7
55% S	3.4 ± 0.1	0.32 ± 0.01	81 ± 1	63 ± 1	69 ± 1	27 ± 2	41.5 ± 0.5
59% S	2.6 ± 0.1	0.20 ± 0.01	81 ± 1	59 ± 1	70 ± 1	25 ± 1	42.6 ± 0.8

Table 3: Contact angle measurements and surface energy calculations for P(S-r-MMA) brushes.

Substrate Neutrality. The following paragraphs describe a simple procedure to test for substrate neutrality. 9,10 Data were acquired at two annealing temperatures to reveal subtle interactions at each interface that control domain orientations. A series of PS-PMMA films with varying thicknesses (in the range of $t=0.5L_0$ to $2.5L_0$) were cast on the brushed substrates and annealed in air for 10 minutes at 240 °C. An additional 6 hours of annealing did not change the results (Figures S3 and S4). All samples were cleaved into two pieces, and one section was further annealed under low vacuum (10 mTorr) for two days at 200 °C. We also analyzed one set of samples (on brushes with $\Sigma=0.2~{\rm nm}^{-2}$) that were prepared without the first annealing step at 240 °C, 9 and these data demonstrate that outcomes are independent of thermal history. All samples were imaged with high resolution AFM or SEM to characterize ordering at the air interface. Each micrograph was analyzed with ImageJ software to identify the area fraction of perpendicular domains at the air interface ($f_{\rm perp}$). Average values of f_{perp} were computed from a minimum of five 5 μ m \times 5 μ m micrographs, and error bars reflect the standard deviation. A representative micrograph is included in Figure S5. Figures 1a and 1b report $f_{\rm perp}$ as a function

of normalized film thickness (t/L_0) , brush grafting density (Σ) , and final processing temperature (200 °C or 240 °C). We note that t/L_0 reflects the as-cast value, and subsequent heating can drive the films to separate into regions with different thicknesses.

The domain orientations exhibit a strong dependence on normalized film thickness t/L_0 at 200 °C. Perpendicular domains ($f_{
m perp}=1$) are observed when film thicknesses are $tpprox nL_0$, where n=1 or 2. Mixed orientations (0 $< f_{
m perp} < 1$) occur at intermediate thicknesses near $t pprox (n \pm 0.2) L_0$. Parallel lamellae ($f_{
m perp} = 0$) with low densities of islands or holes are detected near $t \approx (n + 0.5)L_0$. The heights of islands and depths of holes are approximately equal to the lamellar periodicity of $L_0=46~\mathrm{nm}$ (Figure S6). These data are consistent with asymmetric wetting, where PS is attracted to the air interface and PMMA is preferred at the brushed substrate. 9,10 The attraction of PS blocks to the air interface is well-documented at temperatures below 220°C. 46,50-53 However, adsorption of PMMA at the brushed substrate is a bit surprising: While many studies have shown that PMMA is strongly preferred over PS on an oxidized silicon wafer, 1,50,54 the P(S-r-MMA) brushes are designed to screen those interactions and generate a neutral boundary. 1,11,12 All of the brushes have a higher content of styrene than methyl methacrylate, so brush chemistry is not driving this behavior. One possible explanation is conformational asymmetry in the block copolymer, which favors placement of the more flexible block (smaller Kuhn length) at a neutral boundary. 55,56 (The Kuhn lengths of PS and PMMA are 1.8 nm and 1.5 nm, ⁵⁷ respectively.) Another potential explanation is an enthalpic attraction between PMMA and the oxidized silicon wafer when Σ is low. Such behavior was documented in other studies of PS-PMMA lamellae on pure PS brushes, where perpendicular domains were detected at the surface of the film when Σ was low (ca. $0.15~\mathrm{nm}^{-2}).^{34}$

Annealing at 240 °C promotes a perpendicular orientation of PS-PMMA lamellae ($f_{\rm perp}=1$) at all film thicknesses when the grafting density of the underlying brush is high ($\Sigma \geq 0.4$ nm $^{-2}$). This behavior is consistent with other studies that used elevated processing temperatures to eliminate PS wetting layers at the air interface. Samples prepared on brushes with low grafting density ($\Sigma < 0.4$ cm $^{-2}$) exhibit perpendicular domains in thicker films ($t/L_0 > 1$), but regions of parallel lamellae and a transition to hexagonal perforated lamellae are detected in ultrathin films ($t/L_0 \leq 1$). Examples of these data are included in Figure S7. Transitions to perforated morphologies are often observed in ultrathin block copolymer films that exhibit

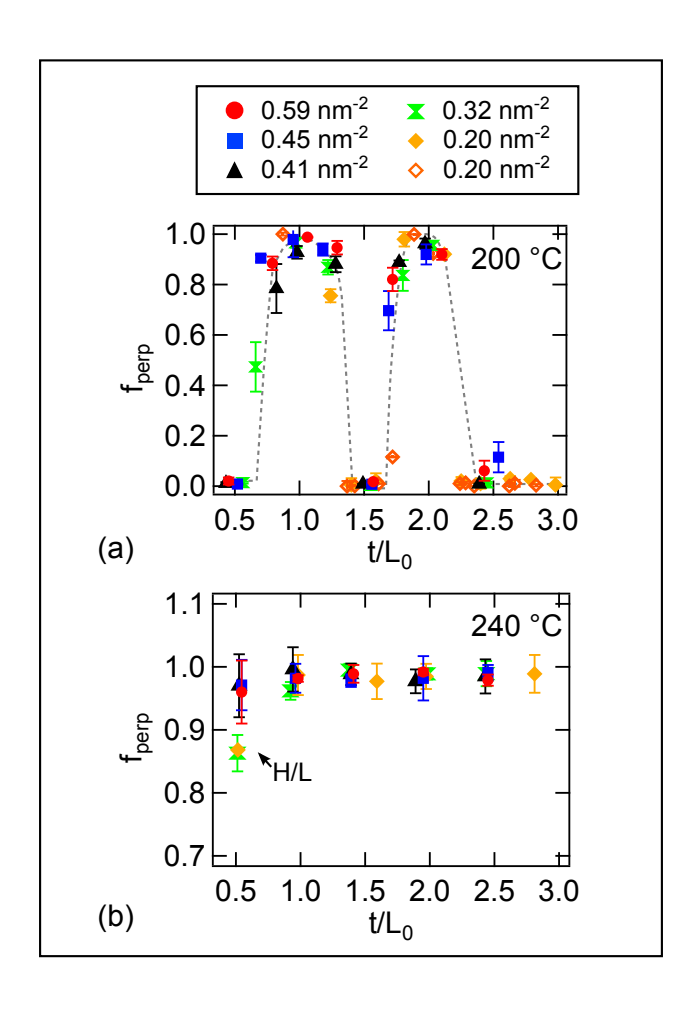


Figure 1: Area fraction of perpendicular lamellae at the air interface. (a) Pre-annealing at 240 °C for 10 min, followed by annealing at 200 °C for 2 days. Open orange diamonds denote samples that were heated at 200 °C without the pre-anneal at 240 °C. The dashed line is a guide to the eye. (b) Annealing at 240 °C for 10 min. H/L = hexagonal and lamellar structures.

preferential interactions at one or both interfaces. 33,58,59

Lateral Order. We examined lateral domain ordering at the top of the film as a function of normalized block copolymer film thickness (t/L_0) and brush grafting density (Σ) using AFM and SEM. These studies are restricted to annealing at 240 °C, as processing at a lower temperature failed to drive perpendicular ordering over a broad range of film thicknesses. The resulting "fingerprint" structure is characterized by dislocations and disclinations that are characteristic of smectic block copolymer phases and produce short-range order. The normalized orientational correlation length (ζ/L_0) was calculated from each micrograph with the algorithm described in

the Experimental Procedures and reported elsewhere. ^{18,19} Representative images are included in Figure 2 for a few values of t/L_0 and Σ , where each grain is colored according to its in-plane orientation. It is clear by visual inspection that ordering is improved with increasing film thickness.

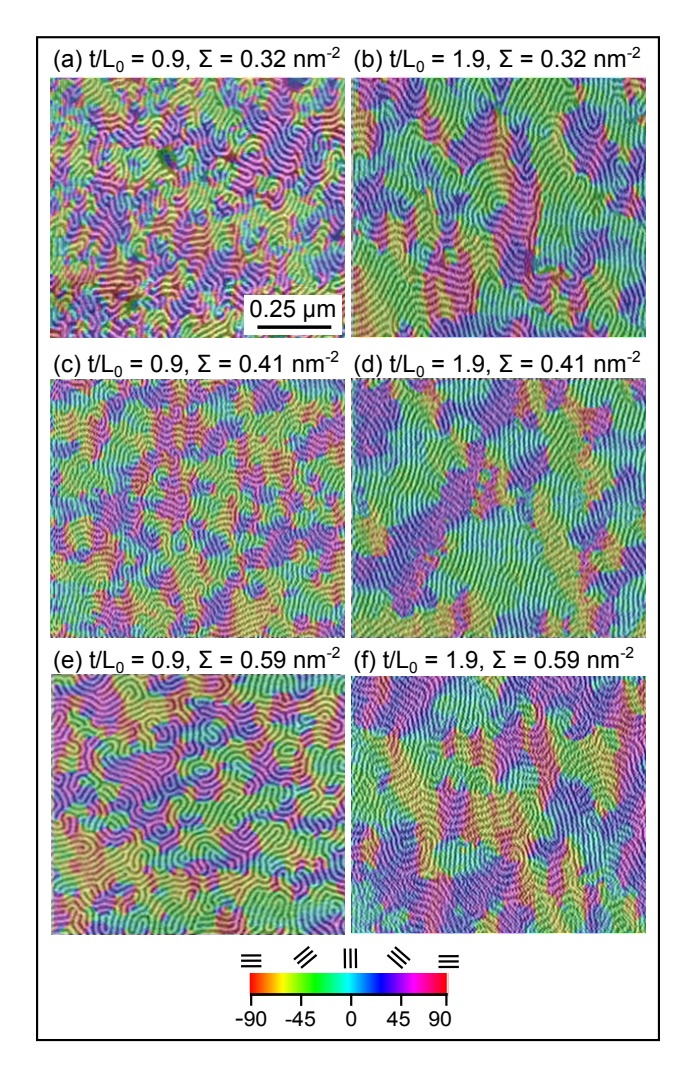


Figure 2: Examples of microscopy measurements for different film thicknesses (t/L_0) and brush grafting densities (Σ) . The grains in each image are colored according to their in-plane orientation.

Figure 3a summarizes ζ/L_0 as a function of t/L_0 for each type of brush (different values of Σ). The symbols in Figure 3a are often larger than the uncertainty of the measurement. To see trends that depend on Σ more clearly, Figure 3b reports ζ/L_0 as a function of Σ for films that have nearly the same thickness. We observe two trends in these data: First, for a fixed block copolymer film thickness, the orientational correlation length generally increases with brush grafting density. This behavior is consistent with other studies of smectic block copolymer phases that show better

lateral order on grafted brushes compared with adsorbed brushes: 26,27 Grafted brushes have higher chain densities per unit area than adsorbed brushes, so they are more effective at screening preferential interactions between a substrate and overlying copolymer film, thereby enhancing the ordering kinetics. Second, for a fixed grafting density, the orientational correlation length increases with block copolymer film thickness. The latter trend is well-described with the simple scaling $\zeta \propto t^n$, and Table 4 summarizes the exponent n for each Σ . Many studies have reported similar improvements in lateral domain order with increasing film thickness, 22,24,25,60 although each study uses different metrics to quantify this behavior. The reported scaling exponents for PS-PMMA lamellae are $n\approx 0.4$ on rough indium tin oxide substrates, 24 $n\approx 0.4$ on brushed substrates, 25 and $n\approx 1$ on crosslinked neutral coatings. For our system, n increases from approximately 0.75 to 1 as Σ decreases from 0.6 nm $^{-2}$ to 0.2 nm $^{-2}$.

Brush	$\Sigma \; (\mathrm{nm}^{\text{-}2})$	n	
55% S	0.59 ± 0.01	0.75 ± 0.06	
55% S	0.45 ± 0.01	0.80 ± 0.06	
55% S	0.41 ± 0.01	0.83 ± 0.11	
55% S	0.32 ± 0.01	0.97 ± 0.15	
59% S	0.20 ± 0.01	1.00 ± 0.07	

Table 4: Scaling exponent n for orientational correlation length as a function of film thickness, i.e., $\zeta \propto t^n$. Exponent is reported for each brush grafting density Σ .

The increase in ζ with t reflects a combination of different physics. The energies of disclinations and dislocations will decrease as film thickness is reduced, so there is a weaker drive for defect annihilation in thin films compared with thick films. ^{22,61} Thin film confinement will restrict the pathways for defect annihilation and suppress these kinetics, ²² and high frustration at the substrate boundary can elevate defect densities. ⁶² Figure 3 shows that all of these effects are exacerbated by strong interactions with the underlying substrate: Brushes with low Σ produce higher defectivity, particularly in ultrathin films, which points to a "pinning" or "trapping" of domains at the substrate. The dependence of the scaling exponent n on Σ may reflect the extent of frustration at the substrate: A strongly pinning substrate will suppress ordering in an

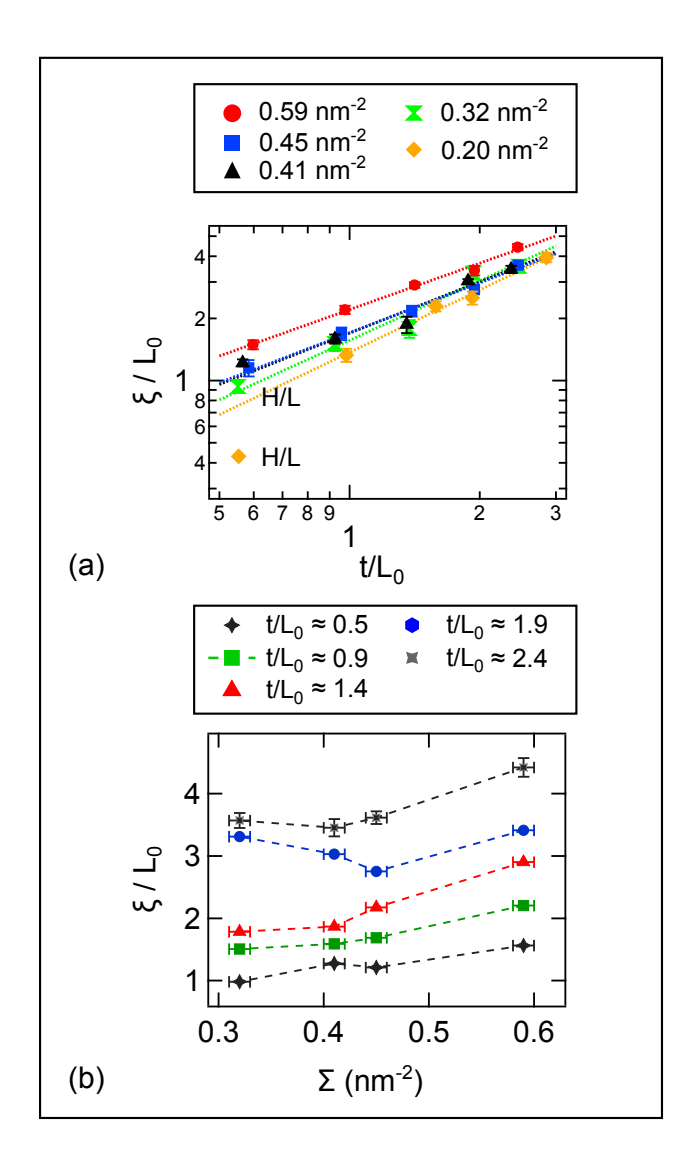


Figure 3: (a) Normalized orientational correlation length (ζ/L_0) at the top of the film as a function of normalized film thickness (t/L_0) . H/L samples exhibit a significant area fraction of hexagonal perforations. Lines are best-fit to a power law $\zeta \propto t^n$ (does not include H/L data points). (b) Normalized orientational correlation length (ζ/L_0) at the top of the film as a function of brush grafting density (Σ) .

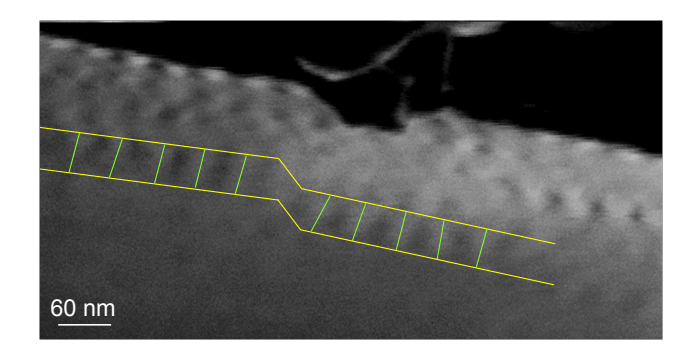


Figure 4: Cross-sectional SEM for normalized film thickness $t/L_0 = 1.4$ and brush grafting density $\Sigma = 0.45 \text{ nm}^{-2}$. Horizontal yelow lines mark the top and bottom interfaces, while vertical green lines denote the approximate domain orientation.

ultrathin film, but have a weaker impact in thicker films where other factors facilitate defect removal, leading to a more rapid increase of ζ with t. Similar behavior has been observed with directed self-assembly of lamellar block copolymers, where the influence of a chemically-patterned substrate on lateral order decays with increasing film thickness. ⁶¹

Out-of-plane Order. Most studies of defect formation in perpendicular lamellar phases have focused on in-plane structure, but these systems have another characteristic dimension that is controlled by the film thickness t. Microscopy is an attractive method to study out-of-plane order in block copolymer films because such "real-space" measurements are easy to understand. However, cross-sectional electron microscopy is significantly more challenging to implement than surface imaging. As an example, Figure 4 displays cross-sectional SEM data for a film with thickness $t/L_0=1.4$ and brush grafting density $\Sigma=0.45$ nm $^{-2}$. Additional images for other samples are included in Figures S8-S10. Each film was etched for a few seconds in an oxygen plasma to enhance contrast between PS and PMMA domains. It is hard to locate regions in a fingerprint pattern where the in-plane lamellar orientation is normal to the cut, and the best images capture less than 15 domains. However, we observe an apparent distribution of domain orientations relative to the interfaces. We did not attempt to quantify this behavior as the image quality is low and the statistics are poor.

We opted to evaluate out-of-plane order (domain orientations) with GISAXS measurements, 9,63 as this technique can rapidly measure large areas. Figure 5 includes representative

GISAXS data for PS-PMMA films with normalized thicknesses of $t/L_0\approx 0.9$ and $t/L_0\approx 1.9$ on brushes with $\Sigma=0.32~{\rm nm^{-2}}$ and $0.59~{\rm nm^{-2}}$. The patterns contain three features that offer qualitative insight into the extent of in-plane and out-of-plane disorder. First, the in-plane line shape of the first-order peak (along the 2Θ axis) is broader in thin films compared with thick films. Line shape is inversely related to orientational correlation length, so these data demonstrate that confinement suppresses lateral order, an outcome that is consistent with the previously discussed surface microscopy data. Figure S11 includes a summary of line shape as a function of film thickness to illustrate this point. Second, the lamellar form factor is "smeared" due to out-of-plane disorder when the brush is very thin, which is seen most clearly by comparing parts c and d. Last, the GISAXS data exhibit partial Debye-Scherrer rings that are associated with misoriented domains, 9,64 meaning lamellae that are tilted relative to the normal axis. The following paragraphs describe two approaches for quantifying the out-of-plane disorder using GISAXS data, as well as the factors that contribute to this type of defectivity. We restrict the analysis to samples that exhibit perpendicular lamellar in surface microscopy (so samples with $t/L_0\approx 0.5$ and $\Sigma<0.4~{\rm nm}^{-2}$ are excluded).

The intensity of the first-order peak (at $2\Theta=0.21^\circ$) along the out-of-plane axis is produced by the intersection of the in-plane structure factor with the lamellar form factor. This "scattering rod" is marked by the arrow in Figure 5 (feature 1). Therefore, by modeling this intensity profile, one can extract a distribution of domain orientations throughout the depth of the film. The GISAXS intensity is modeled using the distorted-wave Born approximation (DWBA), 44,63,65 and the details of this approach are reviewed in the Appendix. Briefly, we assume that perpendicular lamellae propagate throughout the thickness of the film, and the distribution of domain orientations is described by a Gaussian probability density. These parameters are illustrated in Figure 6a. The standard deviation of the Gaussian distribution, σ_{γ} , is an adjustable parameter for regression analysis. Note that $\gamma=0$ denotes a perfectly perpendicular domain, and this is the most probable orientation. Other models for out-of-plane disorder, such as a distribution of domain heights, could not describe the GISAXS data.

The optimal values of σ_{γ} are reported in Figure 6 as a function of normalized film thickness and brush grafting density. The average values and uncertainties were calculated from fits at two angles of incidence ($\alpha^i \approx 0.2^{\circ}$ and 0.22°), and the dashed line in part b) denotes the resolution

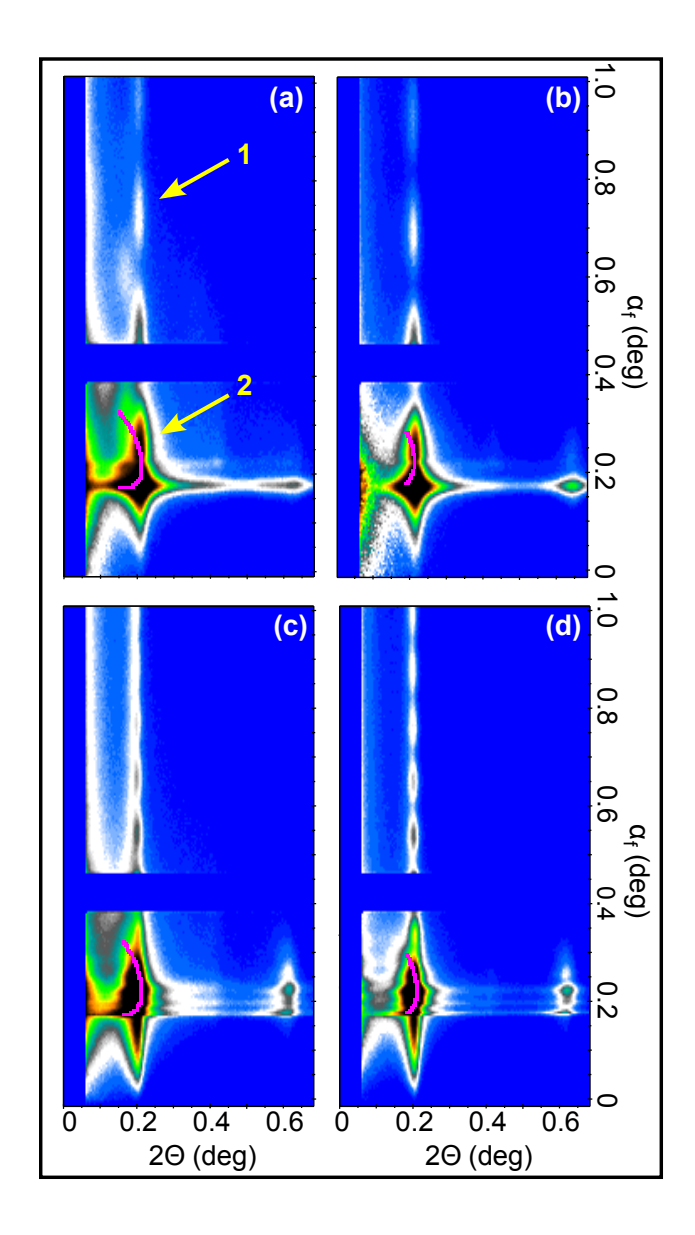


Figure 5: GISAXS patterns for $\alpha^i = 0.22^\circ$. (a) $t/L_0 \approx 0.9$, $\Sigma = 0.32 \text{ nm}^{-2}$; (b) $t/L_0 \approx 0.9$, $\Sigma = 0.59 \text{ nm}^{-2}$; (c) $t/L_0 \approx 1.9$, $\Sigma = 0.32 \text{ nm}^{-2}$; (d) $t/L_0 \approx 1.9$, $\Sigma = 0.59 \text{ nm}^{-2}$. Arrows (1) and (2) indicate the scattering rod and Debye-Scherrer rings, respectively, at the first-order peak ($2\Theta \approx 0.21^\circ$). The second-order peak ($2\Theta \approx 0.42^\circ$) is not observed because it coincides with a minimum in the lamellar form factor.

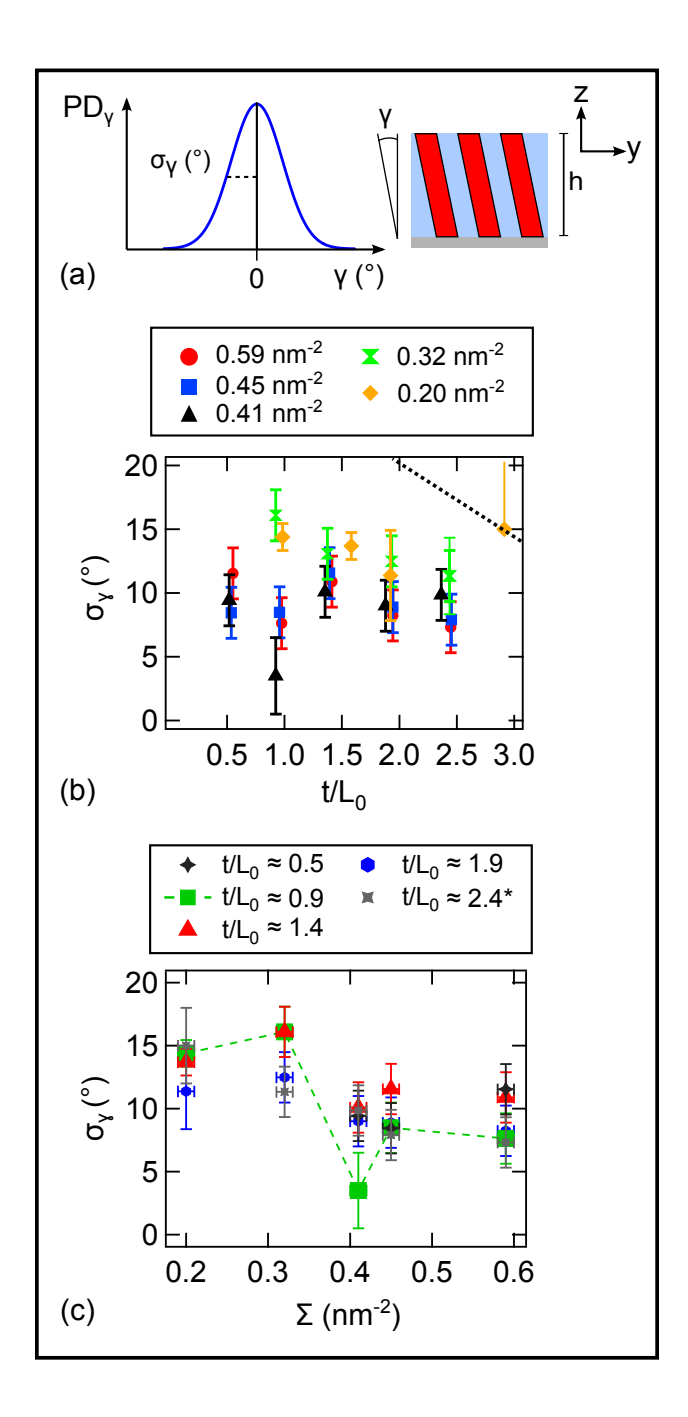


Figure 6: (a) Illustration of domain tilt and Gaussian probability density of tilt angles. (b) σ_{γ} as a function of normalized film thickness t/L_0 . Dashed line marks the resolution limit for this method of analysis. (c) σ_{γ} as a function of brush grafting density Σ . *Note: $t/L_0 = 2.8$ when $\Sigma = 0.2$ nm⁻².

limit for the DWBA model. All samples are characterized by a population of misoriented domains. The dependence of σ_{γ} on thickness and grafting density is rather complex: In ultrathin films $(t/L_0=0.5)$ and thick films $(t/L_0>1.9)$, σ_{γ} is independent of Σ and approximately equal to 10° for both data sets. In films with $t/L_0=0.9$, $\sigma_{\gamma}\approx 8^{\circ}$ when $\Sigma>0.4$ nm⁻² and $\sigma_{\gamma}\approx 15^{\circ}$ when $\Sigma<0.4$ nm⁻². Similar behavior is observed when $t/L_0=1.4$, where $\sigma_{\gamma}\approx 10^{\circ}$ when $\Sigma>0.4$ nm⁻² and $\sigma_{\gamma}\approx 15^{\circ}$ when $\Sigma<0.4$ nm⁻².

It is challenging to calculate domain orientations from GISAXS data using the DWBA framework, because this method requires rocking curves, detailed analysis of XRR data, and a complex scattering theory to build the objective function for regression analysis. Therefore, we compared the DWBA model with a simple approach that is based on analysis of partial powder rings. Referring back to Figure 5, each GISAXS pattern exhibits a partial "Debye-Scherrer" powder ring (labeled as feature 2) that is characteristic of misoriented domains. ^{9,64} The trajectory of these partial rings in $(2\Theta, \alpha^f)$ space was used to calculate the range of misorientation angles through a straightforward procedure: ⁹ First, the scattering vector for misoriented lamellar domains is defined in terms of γ :

$$\vec{q} = \{q_y, q_z\} = \left\{\frac{2\pi}{L_0}, 0\right\} \cdot M_{rot}(\gamma) = \left\{\frac{2\pi}{L_0} \cos[\gamma], -\frac{2\pi}{L_0} \sin[\gamma]\right\}$$
(3)

The function $M_{rot}(\gamma)$ is a 2D rotation matrix in the (y,z) plane. Second, the scattering vector is calculated for the range of angles spanning $\pm \gamma_{max}$, and the corresponding scattering angles (in radians) are determined from Equations (4)-(5):

$$\alpha^f = \arcsin \sqrt{\sin^2[\alpha^i] + \left(\frac{q_z^2 \mp 2q_z k_0 \sqrt{\sin^2[\alpha^i] - \sin^2[\alpha_{c,3}]}}{k_0^2}\right)}$$
 (4)

$$2\Theta \simeq q_y/k_0 \tag{5}$$

The " \mp " term in Equation (4) reflects the different scattering events that are possible in a GISAXS experiment.⁹ The parameter $\alpha_{c,3}$ is the critical angle of the PS-PMMA film, which is approximately 0.17°. Last, the γ -range is refined until the predicted trajectory matches the experimental data. (The trajectory is truncated when the intensity along the partial ring drops to 20% above the background level.) Examples of these comparisons are included in Figure 5. This model does not make assumptions about the shape of domains, so it can capture lamellar bending or uniform tilting, but it does imply that neighboring lamellae have the same orientation.

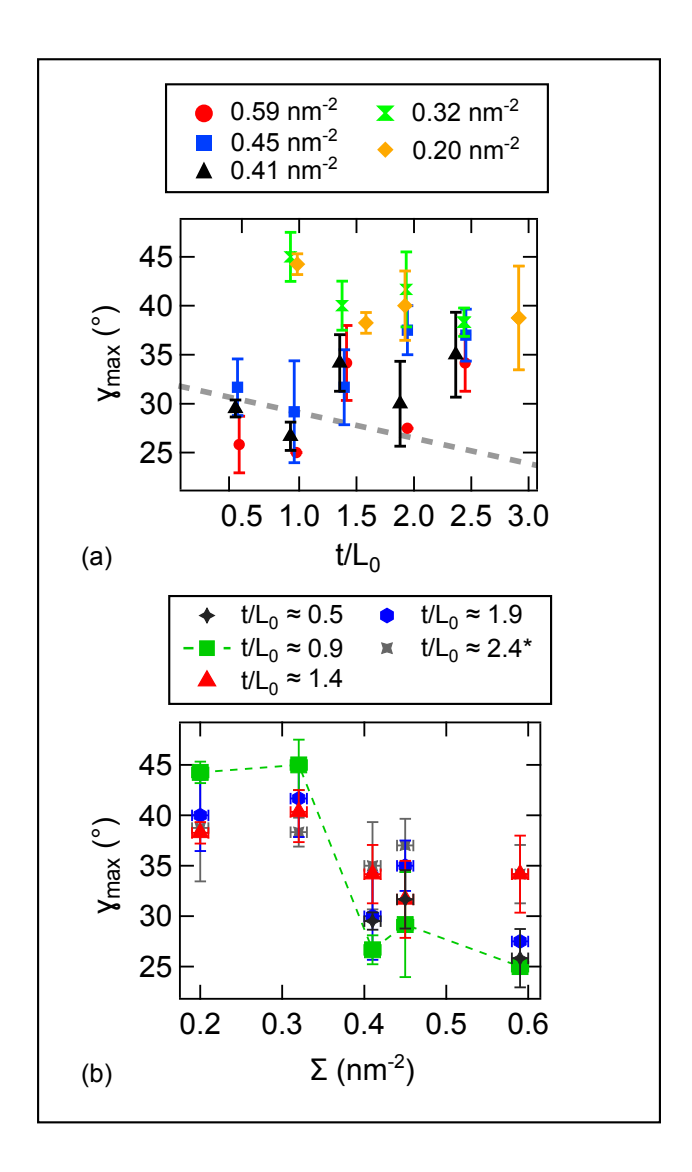


Figure 7: (a) γ_{max} as a function of normalized film thickness t/L_0 . Dashed line marks the resolution limit. (b) γ_{max} as a function of brush grafting density Σ . *Note: $t/L_0 = 2.8$ when $\Sigma = 0.2$ nm⁻².

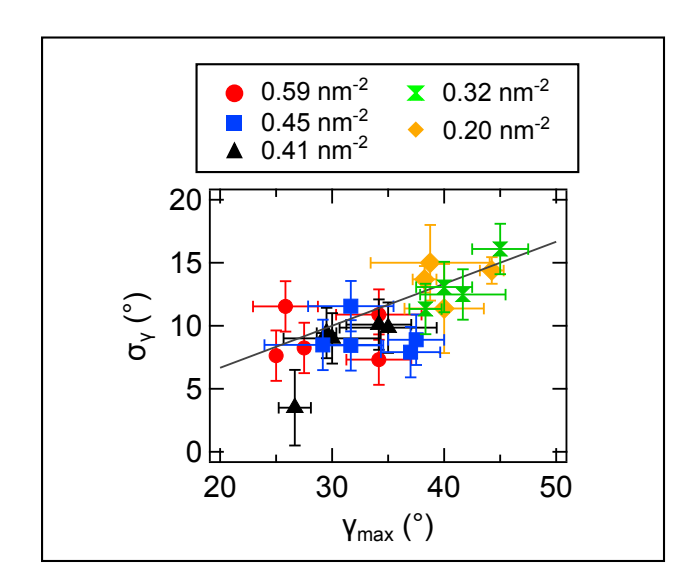


Figure 8: Comparison of DWBA modeling (σ_{γ}) and contour analysis (γ_{max}) The solid line marks $3\sigma_{\gamma} = \gamma_{max}$.

Figure 7(a) summarizes γ_{max} as a function of normalized PS-PMMA film thickness and brush grafting density based on an average for $\alpha^i\approx 0.2^\circ,\ 0.22^\circ$ and 0.24° (error bars denote ± 1 standard deviation). The dashed line marks the resolution limit for this method of analysis, which is a consequence of broad line shapes in ultrathin films that obscure the partial rings (Figure S11). Significantly, this simple approach for interpretation of GISAXS data captured the same trends predicted by rigorous DWBA modeling, such as the greatest extent of out-of-plane disorder when $t/L_0=0.9$ and $\Sigma<0.4$ nm $^{-2}$. Furthermore, the two methods of data analysis are reconciled by noting that $\gamma_{max}\approx 3\sigma_\gamma$, which is expected for distributions that follow Gaussian statistics (Figure 8). Therefore, we propose that out-of-plane disorder can be evaluated by mapping the trajectory of partial Debye-Scherrer rings, which is significant as this method is extremely simple to implement.

Both methods of GISAXS data analysis confirm that perpendicular lamellar phases exhibit disorder along the out-of-plane direction. Such behavior could be very challenging for block copolymer lithography, because the dimensions of patterned features are coupled to domain tilt. ²⁸ There are very few literature studies that discuss out-of-plane disorder in thin films of perpendicular block copolymer lamellae or cylinders, so the underlying physics that drive this behavior are not fully understood. First and foremost, we propose that tilted/bent domains

are thermally generated, much like the in-plane dislocation and disclination defects that are well-documented in perpendicular lamellar phases. Out-of-plane defects will perturb the chain conformations, but the lamellar elastic energy is comparable to thermal energy, 66,67 so the cost of these deformations should be negligible. Other factors may also contribute to out-of-plane defectivity. One work proposed that cylindrical domains will tilt in response to the strain field at dislocation or disclination cores, 28 which implies that out-of-plane and in-plane order are coupled. The lamellar "fingerprint" patterns in Figure 2 are characterized by high densities of topological defects, but while lateral order at the free surface exhibits a strong improvement with increasing film thickness, the distribution of domain orientations does not follow the same trend. Therefore, it is unlikely that similar effects are relevant to the lamellar phases considered in the present study. Other works have proposed that preferential interactions at the interfaces can drive a variety of out-of-plane defects such as deformed domains, 30-32 order-order transitions, 33,68 and bent or tilted domains. 6,9 The analysis of domain orientations at the free surface (f_{perp} in Figure 1) demonstrates that PMMA is very weakly attracted to the substrate. This proposed attraction is consistent with an entropic preference for flexible chains at the substrate, and a slight enthalpic preference for PMMA at the substrate when Σ is low. It is interesting to note that the maximum "disorder" captured by σ_{γ} or γ_{max} is observed in samples with the lowest brush grafting density Σ . Therefore, our data are consistent with the view that preferential interactions with the underlying substrate can exacerbate out-of-plane disorder.

CONCLUSIONS

We examined in-plane and out-of-plane defectivity in thin films of lamellar PS-PMMA copolymers on brushed P(S-r-MMA) substrates. The principal experimental variables are block copolymer film thickness ($t=0.5L_0$ - $2.5L_0$) and brush grafting density ($\Sigma=0.2$ - 0.6 nm⁻²). Films were processed at an elevated temperature of 240 °C, which drives a rapid self-assembly of perpendicular lamellae for a broad range of t and t. First, we calculated the orientational correlation lengths of lamellar domains at the free surface from high resolution AFM and SEM data. These data show that the densities of in-plane defects are reduced with increasing t and high t. Second, using detailed analysis of GISAXS data, we showed that all films are characterized

by out-of-plane defects (tilted domains). The distribution of domain orientations (normal to the substrate) is well-described by a Gaussian function with standard deviation in the range of 8-15°. The extent of out-of-plane disorder does not follow a clear trend with t, but the maximum value was observed in ultrathin films on brushes with low Σ . These studies demonstrate that defectivity in thin films of lamellar copolymers is comprised of in-plane topological defects and out-of-plane domain tilt, with little or no correlation between the two types of disorder. Furthermore, when films are prepared on brushes with low Σ , interactions between PMMA segments and the substrate can trap both in-plane and out-of-plane defects.

ACKNOWLEDGMENT

The authors acknowledge financial support from the Norman Hackerman Advanced Research Program under Grant No. 003652-0017-2011, the National Science Foundation under Grant No. DMR-1151468, and National Science Foundation Grant No. EEC-1002509 (REU, to A.B.). Use of the Advanced Photon Source, an Office of Science User Facility operated for the U.S. Department of Energy (DOE) by Argonne National Laboratory, was supported by the U.S. DOE under Contract No. DE-AC02-06CH11357. The authors thank Dr. Long Chang for assistance with SEM and Dr. Matt Hammond for sharing $g(\vec{r})$ code.

APPENDIX

The GISAXS intensity is modeled using the distorted-wave Born approximation (DWBA), 44,63,65

$$I(2\Theta, \alpha^{f}) = \langle \langle | \sum_{j=2}^{3} \Delta \rho_{j} T_{j}^{f} T_{j}^{i} F_{j}(q_{y}, q_{z,j}^{1}) + \Delta \rho_{j} R_{j}^{f} T_{j}^{i} F_{j}(q_{y}, q_{z,j}^{2}) + \Delta \rho_{j} T_{j}^{f} R_{j}^{i} F_{j}(q_{y}, q_{z,j}^{3}) + \Delta \rho_{j} R_{j}^{f} R_{j}^{i} F_{j}(q_{y}, q_{z,j}^{4}) |^{2} \rangle_{PD_{\gamma}} \rangle_{\Delta \alpha^{i}} * K(2\Theta, \alpha^{f}),$$
 (6)

with out-of-plane scattering vectors

$$k_{z,i}^{i} = -k_0 \left\{ \sin^2 \alpha^{i} - \sin^2 \alpha_{c,i} \right\}^{0.5} \tag{7}$$

$$k_{z,j}^f = +k_0 \left\{ \sin^2 \alpha^f - \sin^2 \alpha_{c,j} \right\}^{0.5}$$
 (8)

$$q_{z,j}^1 = +k_{z,j}^f - k_{z,j}^i (9)$$

$$q_{z,j}^2 = -k_{z,j}^f - k_{z,j}^i (10)$$

$$q_{z,j}^3 = +k_{z,j}^f + k_{z,j}^i (11)$$

$$q_{z,j}^4 = -k_{z,j}^f + k_{z,j}^i. (12)$$

The summation over j in Equation (6) accounts for the scattering from different layers with distinct electron density contrasts of $\Delta \rho_j$. Layer j=2 describes a "bumpy" film surface where the PMMA domains are slightly taller than PS domains (scattering contrast from air/PMMA). Layer j=3 describes the interior film structure, meaning the height and orientation of lamellar domains (scattering contrast from PS/PMMA). This notation for layer indexing comes from the Parratt recursions, ⁴⁰ where layers 1, 4, and 5 are vacuum, native oxide, and bulk silicon, respectively. There is no off-specular scattering from any of these layers, i.e., $\Delta \rho_j=0$, so they do not appear in the DWBA formalism. The transmission and reflection coefficients for incoming ("i") and outgoing ("i") waves in each layer j are $T_j^f(\alpha^f)$, $T_j^i(\alpha^i)$, $R_j^f(\alpha^f)$, and $R_j^i(\alpha^i)$. The scattering potential for the lamellar nanostructures in each layer j is

$$F_j(q_y, q_{z,j}^m) = S(q_y) P_j(q_y, q_{z,j}^m), \tag{13}$$

where $S(q_y) = \delta(q_y - 2\pi n/L_0)$ is the 1D structure factor and $P_j(q_y, q_{z,j}^m)$ is the lamellar form factor. The predicted GISAXS intensity reflects the average over lamellar domain heights and orientations in layer j=3 (denoted by the subscript PD_γ), which is implemented with the local monodisperse approximation, ^{44,69} and includes corrections for incident angle divergence due to wafer curvature (denoted by the subscript $\Delta\alpha^i$). The scattering vectors defined by Equations (7)-(12) for a layer j are a function of the critical angle $\alpha_{c,j}$ and the wave vector modulus $k_0=2\pi/\lambda$. Finally, the DWBA intensity is convolved with a Gaussian resolution function $K(2\Theta,\alpha^f)$ having a standard deviation of 0.0045° (limited by the detector pixel size).

The aim of DWBA analysis is to fit a function for the lamellar form factor to experimental data, thereby determining the out-of-plane domain orientation distribution. All other terms in

the DWBA model are calculated through independent measurements. For example, the incident angle spread is measured with rocking curves as described in the Experimental Procedures, and a representative outcome is reported in Figure 9(a) with the best-fit to Equation (1). The transmission and reflection coefficients in each layer are determined by fitting XRR measurements to the Parratt recursions, which was also described in the Experimental Procedures, and an example of these data is included in Figure 9(b). The scattering contrast for each layer is fixed based on the electron densities of each material. ⁴⁰

To compare GISAXS data with the DWBA model, the diffuse background was subtracted from the first-order peak by fitting a polynomial baseline to each row of the spectra (along the 2Θ axis). A side-by-side comparison of an original and corrected data set is included in Figure 9(c) and Figure 9(d), respectively, for the left and right side of the beam stop (mirror images). We then integrated the first-order peak along the 2Θ axis to produce a line profile $I(\alpha^f)$. Examples of these spectra are included in Figure 10(a-b).

The next step for data analysis is to propose a form factor model that captures the distribution of lamellar domain orientations. The surface structure in layer j=2 is modeled as rectangular protrusions of PMMA with height h_{surf} and width 2w, so the form factor is:

$$P_{2}(q_{y}, q_{z,2}^{m}) = \int_{-h_{surf}}^{0} \int_{-w}^{w} \exp\left[-i\left(q_{y} \cdot y + q_{z,2}^{m} \cdot z\right)\right] dydz$$

$$= 2i \frac{\sin[q_{y}w]}{q_{y}q_{z,2}^{m}} \left(1 - \exp[iq_{z,2}^{m}h_{surf}]\right)$$
(14)

The composition of this PS-PMMA block copolymer is 53% styrene and $L_0=46$ nm, so the width of a PMMA domain is fixed at 2w=22 nm. The protrusion height h_{surf} is an adjustable parameter for optimization. We do not fit a dimension along the x-axis because the lamellar contour length in the fingerprint pattern is too small to detect for our range of α^f ($< 2^{\circ}$).

The PMMA domains in layer j=3 are modeled as rectangular nanostructures with height h and width 2w=22 nm, where the domain orientation γ can vary with respect to the z-axis. We use a Gaussian probability density to describe the distribution of domain orientations. The Gaussian function is centered at $\gamma=0$, meaning perpendicular domains are most probable, and the standard deviation is σ_{γ} . Figure 6(a) illustrates the rectangular nanostructures, tilted orientations,

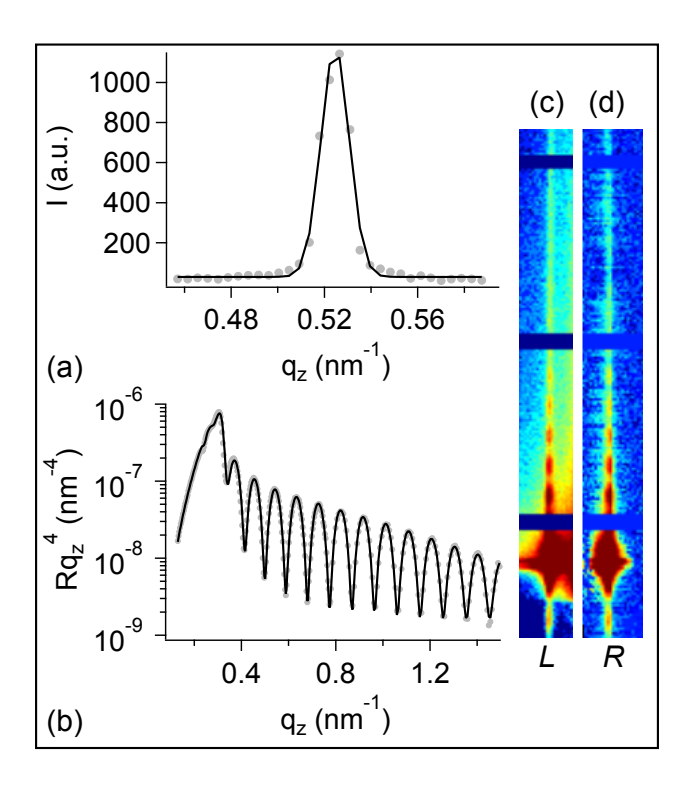


Figure 9: Examples of (a) rocking curve and (b) reflectivity for a PS-PMMA film thickness of $t/L_0 = 1.5$ on a 6.2 nm thick brush ($\Sigma = 0.59 \text{ nm}^{-2}$), with best-fit results for the Gaussian resolution function (Equation 1) and Parratt recursions,³⁹ respectively. The out-of-plane scattering vector is $q_z = 2k_0 \sin(\alpha^f)$. Images (c) and (d) show the first-order peak before and after background correction, respectively, on a logarithmic intensity scale. L and R denote left and right side of the beamstop, i.e., mirror images.

and probability density function. The form factor for the misoriented lamellar domains is:

$$P_{j}(q_{y}, q_{z,3}^{m}) = \int_{-h}^{-h_{surf}} \int_{-w+z\cdot\tan\gamma}^{w+z\cdot\tan\gamma} \exp\left\{-i\left(q_{y}\cdot y + q_{z,3}^{m}\cdot z\right)\right\} dydz$$

$$\simeq \frac{2\sin\left[q_{y}w\right]\left(i-i\cos\left[h\left\{q_{z,3}^{m} + q_{y}\tan\left[\gamma\right]\right\}\right] + \sin\left[h\left\{q_{z,3}^{m} + q_{y}\tan\left[\gamma\right]\right\}\right]\right)}{q_{y}\left(q_{z,3}^{m} + q_{y}\tan\left[\gamma\right]\right)}$$

$$(15)$$

The adjustable parameters for optimization are h and σ_{γ} . This model for out-of-plane disorder is rather simple and does not account for the fact that domains may bend in addition to tilting. However, capturing domain curvature requires a form factor model with additional adjustable parameters, and increased model complexity will produce many degenerate solutions when experimental data are limited to a single well-defined scattering rod. We do not observe

strong higher-order scattering rods along the q_y axis because the lateral ordering is poor, so the GISAXS intensity rapidly decays along the q_y axis, ⁶⁵ and the positions of even-order Bragg peaks $(q_y=2\pi n/L_0,\ n=2,4,...)$ coincide with minima in the lamellar form factor (see Figure 5 and Figure S12). Furthermore, the cross-sectional SEM data are consistent with a uniform tilt model.

For each sample, GISAXS data were acquired at two angles of incidence ($\alpha^i \approx 0.2^\circ$ and 0.22°), and each background-corrected spectra $I(\alpha^f)$ was independently analyzed with the DWBA model. The optimal value of h_{surf} was always very small (ca. 0.2 nm), so the scattering from layer j=2 produces a nearly flat profile along the α^f axis. This effect is similar to adding a constant intensity offset in the objective function. The optimal value of h was typically a few nanometers less than the total film thickness measured by XRR. This outcome is expected because the total film thickness reflects both the PS-PMMA film and underlying brush. The optimal value of σ_γ is reported in the Results and Discussion. The resolution limit of the DWBA analysis is determined by the ability to distinguish the periodic $I(\alpha^f)$ oscillations, where the period in q_z -space is inversely related to domain height. The oscillations in thick films with "tall" domains are smeared when σ_γ exceeds approximately 15°. This smearing is observed in Figure 5(b) and Figure 10(b) when Σ is low.

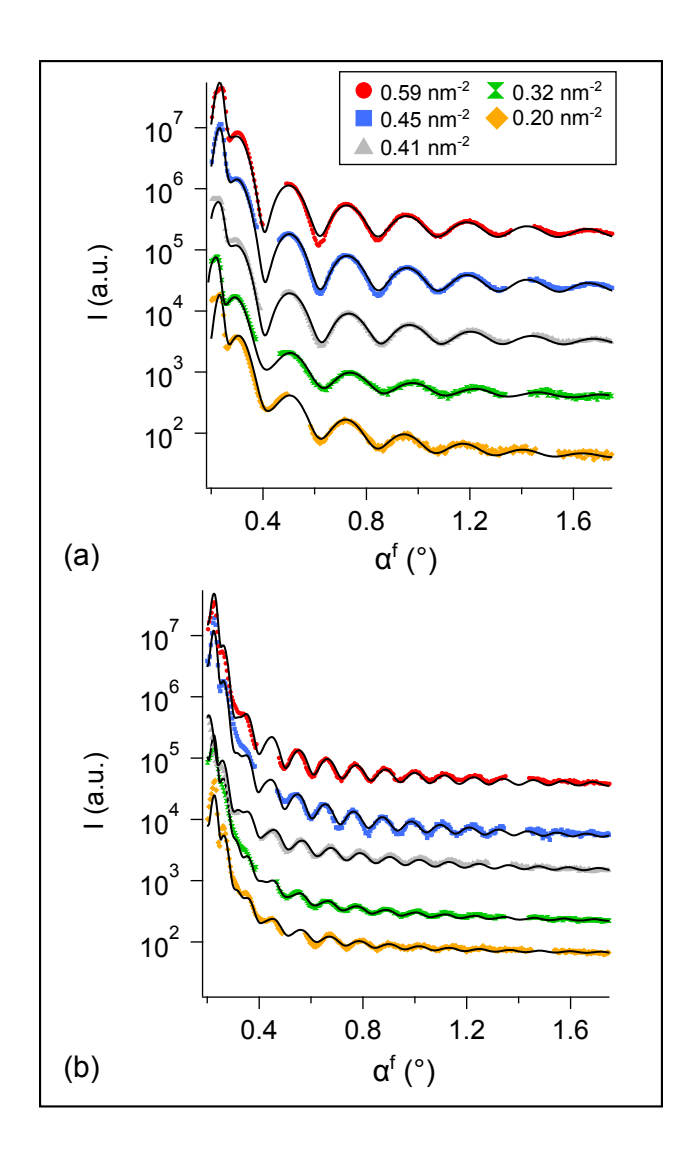


Figure 10: First-order scattering rod as a function of brush grafting density for (a) $t/L_0 = 1$ and (b) $t/L_0 = 2$. Solid black line is the best-fit to the DWBA model ($\alpha^i \approx 0.22^\circ$).

References

- Bang, J.; Jeong, U.; Ryu, D. Y.; Russell, T. P.; Hawker, C. J. Advanced Materials 2009, 21, 4769–4792.
- 2. Bates, C. M.; Maher, M. J.; Janes, D. W.; Ellison, C. J.; Willson, C. G. *Macromolecules* **2014**, *47*, 2–12.
- 3. Ruiz, R.; Kang, H.; Detcheverry, F. A.; Dobisz, E.; Kercher, D. S.; Albrecht, T. R.; de Pablo, J. J.; Nealey, P. F. *Science* **2008**, *321*, 936–939.
- 4. Cheng, J. Y.; Sanders, D. P.; Truong, H. D.; Harrer, S.; Friz, A.; Holmes, S.; Colburn, M.; Hinsberg, W. D. *ACS Nano* **2010**, *4*, 4815–4823.
- 5. Yi, H.; Bao, X.-Y.; Zhang, J.; Bencher, C.; Chang, L.-W.; Chen, X.; Tiberio, R.; Conway, J.; Dai, H.; Chen, Y.; Mitra, S.; Wong, H.-S. P. *Advanced Materials* **2012**, *24*, 3107–3114.
- 6. Liu, C.-C.; Ramirez-Hernandez, A.; Han, E.; Craig, G. S. W.; Tada, Y.; Yoshida, H.; Kang, H.; Ji, S.; Gopalan, P.; de Pablo, J. J.; Nealey, P. F. *Macromolecules* **2013**, *46*, 1415–1424.
- 7. Mansky, P.; Russell, T. P.; Hawker, C. J.; Mays, J.; Cook, D. C.; Satija, S. K. *Physical Review Letters* **1997**, *79*, 237–240.
- 8. Han, E.; Stuen, K. O.; Leolukman, M.; Liu, C.-C.; Nealey, P. F.; Gopalan, P. *Macromolecules* **2009**, *42*, 4896–4901.
- Vu, T.; Mahadevapuram, N.; Perera, G. M.; Stein, G. E. *Macromolecules* 2011, 44, 6121–6127.
- 10. Kim, S.; Bates, C. M.; Thio, A.; Cushen, J. D.; Ellison, C. J.; Willson, C. G.; Bates, F. S. *ACS Nano* **2013**, *7*, 9905–9919.
- 11. Mansky, P.; Liu, Y.; Huang, E.; Russell, T. P.; Hawker, C. J. *Science* **1997**, *275*, 1458–1460.
- 12. Ryu, D.; Shin, K.; Drockenmuller, E.; Hawker, C.; Russell, T. *Science* **2005**, *308*, 236–239.
- 13. Han, E.; Stuen, K. O.; La, Y.-H.; Nealey, P. F.; Gopalan, P. *Macromolecules* **2008**, *41*, 9090–9097.

- 14. Liu, P.-H.; Thébault, P.; Guenoun, P.; Daillant, J. Macromolecules 2009, 42, 9609-9612.
- 15. Albert, J. N. L.; Baney, M. J.; Stafford, C. M.; Kelly, J. Y.; Epps, T. H. *ACS Nano* **2009**, 3, 3977–3986, PMID: 19950910.
- 16. Bates, C. M.; Strahan, J. R.; Santos, L. J.; Mueller, B. K.; Bamgbade, B. O.; Lee, J. A.; Katzenstein, J. M.; Ellison, C. J.; Willson, C. G. *Langmuir* 2011, 27, 2000–2006.
- 17. Harrison, C.; Adamson, D. H.; Cheng, Z. D.; Sebastian, J. M.; Sethuraman, S.; Huse, D. A.; Register, R. A.; Chaikin, P. M. *Science* **2000**, *290*, 1558–1560.
- 18. Harrison, C.; Cheng, Z. D.; Sethuraman, S.; Huse, D. A.; Chaikin, P. M.; Vega, D. A.; Sebastian, J. M.; Register, R. A.; Adamson, D. H. *Physical Review E* **2002**, *66*.
- 19. Hammond, M.; Cochran, E.; Fredrickson, G.; Kramer, E. *Macromolecules* **2005**, *38*, 6575–6585.
- 20. Takahashi, H.; Laachi, N.; Delaney, K. T.; Hur, S.-M.; Weinheimer, C. J.; Shykind, D.; Fredrickson, G. H. *Macromolecules* **2012**, *45*, 6253–6265.
- 21. Mishra, V.; Fredrickson, G. H.; Kramer, E. J. ACS Nano 2012, 6, 2629–2641.
- 22. Campbell, I. P.; Hirokawa, S.; Stoykovich, M. P. *Macromolecules* **2013**, *46*, 9599–9608.
- 23. Choi, S.; Kim, E.; Ahn, H.; Naidu, S.; Lee, Y.; Ryu, D. Y.; Hawker, C. J.; Russell, T. P. *Soft Matter* **2012**, *8*, 3463–3469.
- 24. Sivaniah, E.; Hayashi, Y.; Matsubara, S.; Kiyono, S.; Hashimoto, T.; Fukunaga, K.; Kramer, E. J.; Mates, T. *Macromolecules* **2005**, *38*, 1837–1849.
- 25. Park, S.-M.; Berry, B. C.; Dobisz, E.; Kim, H.-C. Soft Matter 2009, 5, 957-961.
- 26. Harrison, C.; Chaikin, P. M.; Huse, D. A.; Register, R. A.; Adamson, D. H.; Daniel, A.; Huang, E.; Mansky, P.; Russell, T. P.; Hawker, C. J.; Egolf, D. A.; Melnikov, I. V.; Bodenschatz, E. *Macromolecules* **2000**, *33*, 857–865.
- 27. Jung, Y. S.; Ross, C. A. Nano Letters 2007, 7, 2046–2050.

- 28. Bosworth, J. K.; Dobisz, E. A.; Hellwig, O.; Ruiz, R. *Macromolecules* **2011**, *44*, 9196–9204.
- 29. Stein, G. E.; Mahadevapuram, N.; Mitra, I. *Journal of Polymer Science Part B: Polymer Physics* **2015**, *53*, 96–102.
- 30. Trombly, D. M.; Pryamitsyn, V.; Ganesan, V. Macromolecules 2011, 44, 9867-9881.
- 31. Trombly, D. M.; Pryamitsyn, V.; Ganesan, V. Physical Review Letters 2011, 107, 148304.
- 32. Perera, G. M.; Wang, C.; Doxastakis, M.; Kline, R. J.; Wu, W.-l.; Bosse, A. W.; Stein, G. E. *ACS Macro Letters* **2012**, *1*, 1244–1248.
- 33. Ramirez-Hernandez, A.; Suh, H. S.; Nealey, P. F.; de Pablo, J. J. *Macromolecules* **2014**, *47*, 3520–3527.
- 34. Guo, R.; Kim, E.; Gong, J.; Choi, S.; Ham, S.; Ryu, D. Y. Soft Matter 2011, 7, 6920–6925.
- 35. Zhang, X.; Lee, F. K.; Tsui, O. K. C. Macromolecules 2008, 41, 8148-8151.
- 36. Zhao, Y.; Sivaniah, E.; Hashimoto, T. *Macromolecules* **2008**, *41*, 9948–9951.
- 37. Ham, S.; Shin, C.; Kim, E.; Ryu, D.; Jeong, U.; Russell, T.; Hawker, C. *Macromolecules* **2008**, *41*, 6431–6437.
- 38. Jiang, Z.; Li, X.; Strzalka, J.; Sprung, M.; Sun, T.; Sandy, A. R.; Narayanan, S.; Lee, D. R.; Wang, J. *Journal of Synchrotron Radiation* **2012**, *19*, 627–636.
- 39. Parratt, L. G. *Physical Review* **1954**, *95*, 359–369.
- 40. Tolan, M. X-Ray Scattering from Soft-Matter Thin Films: Materials Science and Basic Research; Springer Tracts in Modern Physics, 1999.
- 41. Brown, D.; Kienzle, P. https://www.ncnr.nist.gov/resources/activation/.
- 42. Wu, S. Journal of Polymer Science Part C: Polymer Symposia 1971, 34, 19.
- 43. Wu, S. Journal of Adhesion 1973, 5, 39-55.
- 44. Jiang, Z.; Lee, D.; Narayanan, S.; Wang, J.; Sinha, S. Physical Review B 2011, 84.

- 45. Welander, A. M.; Kang, H.; Stuen, K. O.; Solak, H. H.; Mueller, M.; de Pablo, J. J.; Nealey, P. F. *Macromolecules* **2008**, *41*, 2759–2761.
- 46. Wu, S. The Journal of Physical Chemistry 1970, 74, 632-638.
- 47. Kitazaki, Y.; Hata, T. The Journal of Adhesion 1972, 4, 123-132.
- 48. Dann, J. Journal of Colloid and Interface Science 1970, 32, 302-320.
- 49. Jańczuk, B.; Białlopiotrowicz, T. *Journal of colloid and interface science* **1989**, *127*, 189–204.
- 50. Coulon, G.; Russell, T. P.; Deline, V. R.; Green, P. F. Macromolecules 1989, 22, 2581-2589.
- 51. Anastasiadis, S.; Russell, T.; Satija, S.; Majkrzak, C. *Physical Review Letters* **1989**, *62*, 1852–1855.
- 52. Russell, T.; Coulon, G.; Deline, V.; Miller, D. Macromolecules 1989, 22, 4600-4606.
- 53. In our experiments, all samples with parallel lamellae at the free surface produce a water contact angle of $(90\pm1)^{\circ}$, confirming the formation of a PS wetting layer at the air interface.
- 54. Green, P. F.; Russell, T. P. *Macromolecules* **1992**, *25*, 783–787.
- 55. Sikka, M.; Singh, N.; Karim, A.; Bates, F.; Satija, S.; Majkrzak, C. *Physical Review Letters* 1993, 70, 307–310.
- 56. Nikoubashman, A.; Register, R. A.; Panagiotopoulos, A. Z. *Macromolecules* **2014**, *47*, 1193–1198.
- 57. Rubinstein, M.; Colby, R. H. Polymer Physics; Oxford University Press, 2003.
- 58. Luo, M.; Seppala, J. E.; Albert, J. N. L.; Lewis, R. L.; Mahadevapuram, N.; Stein, G. E.; Epps, T. H. *Macromolecules* **2013**, *46*, 1803–1811.
- 59. Ahn, H.; Shin, C.; Lee, B.; Ryu, D. Y. *Macromolecules* **2010**, *43*, 1958–1963.
- 60. Ji, S.; Liu, C.-C.; Liao, W.; Fenske, A. L.; Craig, G. S. W.; Nealey, P. F. *Macromolecules* **2011**, *44*, 4291–4300.

- 61. Welander, A. M.; Craig, G. S. W.; Tada, Y.; Yoshida, H.; Nealey, P. F. *Macromolecules* **2013**, *46*, 3915–3921.
- 62. Janes, D. W.; Thode, C. J.; Willson, C. G.; Nealey, P. F.; Ellison, C. J. *Macromolecules* **2013**, *46*, 4510–4519.
- 63. Stein, G.; Kramer, E.; Li, X.; Wang, J. *Macromolecules* **2007**, *40*, 2453–2460.
- 64. Mueller-Buschbaum, P.; Maurer, E.; Bauer, E.; Cubitt, R. *Langmuir* **2006**, *22*, 9295–9303.
- 65. Lee, B.; Park, I.; Yoon, J.; Park, S.; Kim, J.; Kim, K.; Chang, T.; Ree, M. *Macromolecules* **2005**, *38*, 4311–4323.
- 66. Wang, Z. G. Journal of Chemical Physics 1994, 100, 2298–2309.
- 67. Wilmes, G. M.; Durkee, D. A.; Balsara, N. P.; Liddle, J. A. *Macromolecules* **2006**, *39*, 2435–2437.
- 68. Perego, M.; Lupi, F. F.; Ceresoli, M.; Giammaria, T. J.; Seguini, G.; Enrico, E.; Boarino, L.; Antonioli, D.; Gianotti, V.; Sparnacci, K.; Laus, M. *Journal of Materials Chemistry C* **2014**, *2*, 6655–6664.
- 69. Renaud, G.; Lazzari, R.; Leroy, F. Surface Science Reports 2009, 64, 255-380.

Graphical TOC Entry

We investigate the defectivity in perpendicular poly(styrene-b-methyl methacrylate) (PS-PMMA) lamellae on brushed poly(styrene-r-methyl methacrylate) silicon substrates. The in-plane correlation length ζ , which is controlled by the density of topological defects, improves with increasing film thickness t and high brush grafting density Σ . Out-of-plane defects (tilted domains) are detected in all samples, and their distributions are largely independent of t and weakly influenced by Σ . These data reveal the three-dimensional nature of defectivity in perpendicular lamellar phases.

